Wing mechanosensory modulation of optic flow-sensitive descending neurons in butterflies

Julie Lin[1*], Jack A. Supple[1*], Holger G. Krapp[1], Huai-Ti Lin[1]

[1] Department of Bioengineering, Imperial College London, South Kensington, London SW7 2AZ, UK

*These authors contributed equally to this work

Abstract

Visual motion processing in flying insects is strongly modulated by behavioural state, yet the mechanisms by which mechanosensory feedback contributes to this modulation remain poorly understood. Here we show that wing mechanosensation alone is sufficient to modulate a subset of optic-flow–sensitive descending neurons (WFDNs) in butterflies. Airflow stimulation of the wings, mimicking flight conditions, increased baseline firing rates and reduced response latencies in WFDNs, without altering response gain or temporal frequency tuning. These effects indicate that mechanosensory modulation acts through mechanisms distinct from those governing other state-dependent changes in visual processing. Consistent with this interpretation, previous work has shown that baseline firing and response latency can be rapidly modulated, whereas gain changes arise through slower neuromodulatory pathways. Mechanosensory modulation was cell-type specific: the horizontally tuned $\mathrm{WFDN_L}$ neuron was consistently affected across individuals, whereas other WFDN types were largely insensitive, likely reflecting the unilateral airflow stimuli used here. Interestingly, $\mathrm{WFDN_L}$ modulation arose exclusively from mechanosensory input from the proximal area of the wing, not from distal wing deformation. This suggests that descending visual pathways require only coarse gain or excitability modulation rather than detailed information about wing shape or strain, leaving fast reflexive control of distal wing deformation to local ganglionic circuits. Together, our results demonstrate that wing mechanosensation selectively modulates visual descending pathways by altering excitability and timing rather than visual feature encoding, supporting the existence of multiple, parallel mechanisms for state-dependent visual modulation during flight.

Introduction

Insect flight depends on rapid closed-loop control under variable aerodynamic and inertial disturbances, requiring continuous sensory feedback about body motion and wing mechanics. Because flying insects exhibit little passive stability, they rely heavily on active stabilisation supported by multimodal sensory feedback (Taylor and Krapp, 2007). This feedback includes vision (compound eyes and ocelli (Hardcastle and Krapp, 2016)), airflow sensing (antennae and wind-sensitive hairs (Budick et al., 2007)), inertial sensing (e.g., dipteran halteres (Mohren et al., 2019)), and wing-load/strain sensing (Aiello et al., 2021; Yarger et al., 2025). Importantly, these modalities do not operate entirely in parallel, but are often integrated to maximise system-level precision and dynamic range (Taylor and Krapp, 2007).

Numerous examples demonstrate sensory integration from modalities differing in speed and precision (Hengstenberg, 1993; Schwyn et al., 2011; Sherman and Dickinson, 2004; Parsons et al., 2010). For example, vision provides rich global information about self-motion through optic flow, but is most effective at lower temporal frequencies due to the delays inherent in motion detection (Taylor and Krapp, 2007). In contrast, mechanosensation can remain effective at higher temporal frequencies, but when used to infer orientation they can be subject to bias/temporal drift, which can be corrected by slower visual feedback (Fabian et al., 2024; Verbe et al., 2020). System-level operational range can therefore be extended by combining visual and mechanosensory pathways, as is indeed observed in the flight stabilisation reflexes of many insect species (Dahake et al., 2018; Hengstenberg, 1993).

A prominent centre for multimodal integration in the insect nervous system is the population of descending neurons (DNs) that project from the brain to thoracic motor centres (Gronenberg and Strausfeld, 1990; Namiki et al., 2018). DNs sensitive to wide-field optic flow (WFDNs) coordinate stabilisation reflexes that counter unexpected perturbations to self-motion (Supple et al., 2026; Suver et al., 2016; Wertz et al., 2009a). WFDNs have been described in several species (Ibbotson and GOODMAN, 1990; Nicholas et al., 2020; Olberg, 1981; Rowell and Reichert, 1986; Strausfeld and Bassemir, 1985; Suver et al., 2016; Supple et al., 2026) and primarily receive input from optic flow-sensitive interneurons projecting from the optic lobe (Haag et al., 2007; Strausfeld and Bassemir, 1985; Wertz et al., 2008). In flies, a population of lobula plate tangential cells (LPTCs) are matched to specific patterns of optic-flow (Krapp and Hengstenberg, 1996) and form electrical synapses with WFDNs (Haag et al., 2007; Strausfeld and Bassemir, 1985), which retain this optic flow selectivity (Wertz et al., 2009b). WFDNs are often multimodal, combining additional indicators of self-motion, such as antennal and neck movements (Olberg, 1981). In blowflies, WFDNs also combine visual information from separate sensors, the compound eyes and ocelli (Haag et al., 2007; Strausfeld and Bassemir, 1985; Wertz et al., 2008). Although less resolved than compound eyes, ocelli are faster, and their convergence onto WFDNs effectively reduces the latency of compound eye inputs (Parsons et al., 2010).

Whilst multimodal integration provides one mechanism to extend dynamic range, individual modalities are also subject to state-dependent modulation that shifts their operation range to meet context-dependent requirements (Longden and Krapp, 2009;

Maimon et al., 2010). For example, motion vision in flies is actively tuned by behavioural context (Longden et al., 2014; Maimon et al., 2010; Tuthill et al., 2014). LPTCs show increased response gain to the same visual motion stimuli during locomotion compared to stationary animals (Longden et al., 2014; Maimon et al., 2010). Similarly, walking and flying shifts LPTC frequency tuning to progressively higher image speeds, consistent with matching visual sensitivity to the faster temporal dynamics of sensory feedback during movement (Chiappe et al., 2010; Jung et al., 2011; Longden et al., 2014). These changes are also accompanied by elevated baseline membrane potentials (Maimon et al., 2010) and firing rates (Jung et al., 2011), reduced response latencies, and increased information rates (Longden and Krapp, 2010, 2009).

State-dependent modulation of motion vision is linked to octopaminergic modulation (Longden and Krapp, 2010; Suver et al., 2012). In *Drosophila*, octopaminergic neurons projecting to the optic lobes are necessary and sufficient to produce locomotion-like changes in LPTC activity (Suver et al., 2012). However, multiple mechanisms are likely to be involved. In *Drosophila* LPTCs, changes in baseline membrane potential are not reproduced by octopaminergic application (Suver et al., 2012), and follow much faster dynamics than other octopamine-related changes in visual gain (Maimon et al., 2010). Furthermore, nutritional deprivation counteracts locomotion-related modulation of motion vision to conserve energy, although locomotion-related latency decrements remain unaffected (Longden et al., 2014). Together this suggests that modulation of visual processing is implemented via multiple mechanisms.

Multi-modal convergence may serve as an additional mechanism supporting state-dependent modulation of sensory processing (Rimniceanu et al., 2023; Santer et al., 2006; Wasserman et al., 2015) . Past work has described multi-modal integration in the context of maximising sensor accuracy and precision (Olberg, 1981; Parsons et al., 2010) but less is known about whether and how separate modalities signal changes in e.g. locomotor state. Ascending neurons (ANs) convey information from thoracic ganglia to the brain and are thought to transmit proprioceptive and motor related information to cephalic sensory circuits (Chapman et al., 2018; Chen et al., 2023; Cheong et al., 2024; Fujiwara et al., 2022). ANs may be involved in activating octopamine signalling (Suver et al., 2012) and could produce other changes such as shifts in baseline activity and latency reduction. However, DNs may also provide a more direct target to quickly integrate thoracic and cephalic sensory information.

We hypothesised that airflow across the wings may serve as an indicator of self-motion that modulates visual processing in a similar fashion to that described for octopamine application (Longden and Krapp, 2010). Airflow is a plausible modulator because insect wings are not only actuators but also surfaces for distributed sensors. Whole-wing mapping demonstrates dense mechanosensor arrays with organised spatial patterning and wiring, positioned to sample both airflow-related inputs and deformation mechanics (Fabian et al., 2022; Stanchak et al., 2024; Yoshida and Emoto, 2011). Across insects, campaniform sensilla (CS) transduce local cuticular strain (Aiello et al., 2021), and their placement across the wing constrains what mechanical variables can be encoded (Stanchak et al., 2024).

In this study we investigated the effect of wing airflow mechanosensation on visual DNs in butterflies (Zhan et al., 2024). Butterflies are notable for their unusual style of flight compared with other insect species, with unusually large wings and a correspondingly low wing beat frequency in the range of 10-15Hz (Fei and Yang, 2016; Johansson and Henningsson, 2021; Srygley and Thomas, 2002). Butterflies frequently engage in gliding as well as flapping flight (Harris et al., 1999; Stylman et al., 2020), such that airflow across the wings in the absence of active flapping may be a frequently encountered and dynamically relevant sensory feature. We therefore investigated whether wing airflow mechanosensation modulates butterfly WFDN responses under otherwise quiescent conditions.

Results

Wing airflow modulates spike rates for select WFDN cell types

To investigate the integration of visual and wing mechanosensory information in DNs, we measured extracellular action potentials from the cervical connective and presented moving gratings in the frontal visual field with and without airflow across the wings (Figure 1A-B). Wings were immobilised in an open configuration, secured laterally with the leading edge approximately perpendicular to the body axis (Figure 1A). We removed the stalk and heavily waxed the base of the antennae to prevent previously described antennal mechanosensory inputs to DNs . We focussed on recording WFDNs, and the most frequently encountered was sensitive to horizontal motion towards the ipsilateral side (i.e. lateral, WFDN_L; Figures 1C&2A; (Supple et al., 2026)). Other WFDNs sensitive to horizontal motion in the opposite (medial) direction (WFDN_M, Figure 2B), or to ventral-to-dorsal (dorsal) or dorsal-to-ventral (ventral) motion (WFDN_D/WFDN_V, Figure 2B-C) were also recorded.

WFDN_L showed a statistically significant increase in mean spike rate when visual motion was combined with aeroelastic wing deformation (paired t-test; Bonferroni-corrected $p = 5\times10^{-4}$; N=9 animals). WFDN_L mean spike rate increased by 11.3±4.5 spikes/s, from 17.6±6.5 to 29.0±9.7 spikes/s (mean±std; Figure 2E). Whilst WFDN_D showed a subtle increase in mean spike rate from 6.4±3.1 to 8.1±3.9 spikes/sec, this was statistically insignificant (paired t-test; Bonferroni-corrected p=0.47, N=4 animals). There was no consistent change in mean spike rates for WFDN_M/WFDN_V visual responses with airflow (WFDN_M: 9.0±4.6 to 12.4±3.2, and WFDN_V: 10.1±6.1 to 10.7±6.6 spikes/sec for visual responses without and with airflow, respectively). Notably, one WFDN_M neuron did exhibit a substantial increase in spike rate with airflow akin to WFDN_L; however, this was only observed once (dashed curve, Figure 2B). Furthermore, differences in WFDN airflow sensitivity were also observed within individuals, such that modulations in $WFDN_L$ were seen alongside airflow-insensitive $WFDN_V$ within the same preparation (Figure 1C-D).

Wing airflow does not alter optic flow processing

Changes in locomotive (Maimon et al., 2010; Suver et al., 2012; Longden et al., 2014) and even nutritional state (Longden et al., 2014) have previously been shown to alter properties of motion vision in flies. For example, LPTC response gain (i.e. the difference in response between the preferred and anti-preferred motion directions) increases (Maimon et al., 2010), and visual temporal frequency tuning shifts towards higher image velocities during flying (Suver et al., 2012) or walking (Longden et al., 2014). To test whether aeroelastic WFDN response modulation similarly alters optic flow processing, we compared visual motion directional response gain (Figure 2F) and visual temporal frequency tuning (Figure 2G-L), without/with wing airflow.

There was no statistically significant difference in visual directional response gain for any WFDN type after correcting for multiple comparisons (paired t-test; Bonferroni-corrected $p>0.05$; Figure 2F). $WFDN_D$ did display a consistent but subtle increase in directional motion response gain from 14.9±5.8 spikes/sec without airflow to 16.4±6.0 spikes/sec with airflow; however, this was statistically insignificant after correcting for multiple comparisons (paired t-test; unadjusted $p=0.007$, Bonferroni-corrected $p=0.06$; Figure 2F).

As seen with responses to different gratings directions (Figure 2F), visual temporal frequency tuning showed a statistically significant baseline shift in average spike rates across a range of temporal frequencies for visuo-mechanosensory $WFDN_L$ (Figure 2K; mean $WFDN_L$ spike rate: 22.4±6.5 and 34.6±8.0, without/with airflow, respectively; Bonferroni-corrected $p=4.3\times10^{-4}$). Other WFDN types did not display any statistically significant difference in average spike rate offset. However, similar to that observed for directional tuning, one of our recorded $WFDN_M$ cells did exhibit a substantially increased mean spike rate when airflow was applied (4.7 to 15.0 spikes/sec, without/with airflow; dashed line, Figure 2H).

There was no statistically significant difference in the visual temporal frequency producing the maximum spike rates between airflow and no-airflow conditions, for any WFDN type (paired t-test; Bonferroni-corrected $p>0.5$; Figure 2L). Whilst airflow increased the baseline of $WFDN_L$ responses, the preferred temporal frequency was unchanged (9.1±2.2 and 10.0±4.0 cycles/sec, without/with airflow, respectively). Interestingly, whilst horizontal and ventral WFDNs had preferred temporal frequencies of ~10 cycles/sec (without airflow: $WFDN_L$: 9.1±2.2, $WFDN_M$: 8.8±2.5, and $WFDN_V$: 7.9±4.0 cycles/sec), $WFDN_D$ had a substantially higher preferred temporal frequency of 26.8±1.8 cycles/sec (Figure 2L).

Wing airflow-induced spike rate modulation reduces visual latency

We next investigated whether airflow-induced increases in baseline firing affect visual response latency (Figure 3). We hypothesised that an increased synaptic drive from wing afferents shifts WFDN membrane potential closer to spike threshold, such that visual inputs require less time to elicit a threshold crossing and therefore reducing response latency.

Response latency was estimated from the temporal offset between the peak of the spike-triggered average (STA) grating velocity and spike time. Gratings moved in the preferred direction with a band-limited Gaussian noise velocity profile, presented with and without airflow applied to the wings (Figure 3A–B). As expected, STAs of grating velocity conditioned on spike times show a sharp increase in velocity shortly before the spike (Figure 3C). For $\mathrm{WFDM_L}$, the latency between the peak grating velocity and spike time was 36.6±3.7 ms without airflow and 33.7±4.3 ms with airflow, a statistically significant decrease of 2.9±2.2 ms (i.e. -7.9%, paired t-test; p=0.04; N=5 animals; Figure 3D). In contrast, $\mathrm{WFDN_V}$ had no difference in response latency with and without airflow (without airflow: 39.0±7.3 ms; with airflow: 36.8±5.9 ms; paired t-test p=0.51; Figure 3D).

Mechanosensory input to $\mathrm{WFDN_L}$ derives from the wing base

We next investigated the properties of wing mechanosensory input to $\mathrm{WFDN_L}$ (Figure 4). We first used localised, frequency-modulated sinusoidal airflow to identify the wing region and vibration frequency that elicited the strongest responses (Figure 4A-B). $\mathrm{WFDN_L}$ showed no response to stimulation in the distal forewing (Figure 4Bi, pink) but was tuned to ~60 Hz stimulation at the forewing base (full width at half maximum: 35-105 Hz; N=2 animals; Figure 4Bi, blue). In contrast, mechanosensitive-only interneurons recorded from the meso-thoracic ganglion responded to stimulation in the distal forewing (Figure Bii, pink) with a preferred frequency of 80 Hz (full width at half maximum: 30-190 Hz; N=2 animals).

To further explore how neuronal mechanosensitivity correlated with the aeroelastic wing deformation under the bulk airflow used in our previous experiments (Figures 1-3), we investigated the relationship between neural responses and steady-state wing deformation from high-speed videos (Figure 4C-F). We first decomposed wing deformation using principal component analysis (PCA; Figure 4C). The first 3 principal components (PCs) captured ~90% of wing deformation variance, with most movement occurring at the distal forewing (Figure 4C-D). PC1 deformation contained power across a broad range of frequencies until attenuating above 80 Hz (Figure 4Di), whilst PC2-3 deformation was focused at 80 Hz and 100 Hz, respectively (Figure 4Dii-iii). We next calculated STAs of wing deformation PCs 1-3 for $\mathrm{WFDN_L}$ and ganglion interneurons (Figure 4E-F). In contrast to our localised airflow stimuli, we did not observe any clear correlation between spike timing and these three highest PCs, for either WFDNL or the ganglion interneuron (Figure 4E-F).

Discussion

State-dependent modulation of neural processing reflects a general computational strategy whereby the system-level dynamic range is extended by shifting the relatively narrow operation range of individual neurons to meet context-dependent requirements. In Diptera, changes in internal state - such as locomotion activity or satiation status - modulate optic flow processing in both graded (Maimon et al., 2010) and spiking (K. D. Longden et al., 2014) LPTCs. Locomotion-related modulation produces a variety of changes that shift visual processing toward a faster operating regime, consistent with the increased temporal dynamics of sensory feedback during movement (Maimon et al., 2010). These include increased visual gain (Maimon et al., 2010), a shift in temporal-frequency tuning toward higher image velocities (Jung et al., 2011), elevated baseline membrane potential (Maimon et al., 2010) and firing rates (K. D. Longden et al., 2014), shortened response latencies, and increased information rates (Longden and Krapp, 2010).

Our results align with these previous findings by demonstrating modulation of optic flow-sensitive DNs during mechanosensation of wing airflow, which would occur during flight (Figures 1-3). Notably, mechanosensory-induced modulation was limited to increased baseline firing rates (Figure 2E,K) and shortened response latencies (Figure 3) for WFDN$_L$. It did not change other properties of visual motion detection such as directional preference, response gain (Figure 2F) or temporal frequency tuning (Figure 2L). This suggests that latency modulation arises from separate mechanisms to the modulation of other properties of optic flow processing. Indeed, in *Drosophila*, changes in baseline membrane potential are rapid, closely following flight state (Maimon et al., 2010), whilst flight-induced elevation of visual gain has slower dynamics arising from octopamine neuromodulation (Suver et al., 2012). Similarly, nutritional deprivation elicits energy-conserving constraints on locomotion-related modulation, including cancellation of increased baseline firing rates and response gain, whilst locomotion-related latency decrements remain unaffected (Longden et al., 2014). Our finding that wing mechanosensation effects baseline firing and response latency, but not response gain or temporal frequency tuning, further suggests that multiple mechanisms underly state-dependent changes in visual processing.

Motion detection first occurs in optic lobe T4/T5 cells, which receive dendritic inputs from the medulla/lobula, respectively (Fischbach and Dittrich, 1989; Maisak et al., 2013). Visual gain modulation likely depends on a range of mechanisms including changes in presynaptic excitation and inhibition (Longden and Krapp, 2010; Tuthill et al., 2014). Temporal frequency tuning is determined primarily by the delay time constants of elementary movement detection (Harris et al., 1999; Jung et al., 2011; Strother et al., 2018). Changes in optic flow processing therefore requires modulating these upstream neurons located in the optic lobe (Strother et al., 2018; Tuthill et al., 2014). In contrast, elevated baseline firing and latency reduction can both be achieved by increasing the resting membrane potential of a given neuron closer to spike threshold (Maimon et al., 2010; Santer et al., 2006; Tuthill et al., 2014). Whilst ascending mechanosensory information has been shown to modulate LPTCs (Cheong et al., 2024; Fujiwara et al., 2022, 2017), DN subthreshold membrane potential could be modulated directly by synaptic input within the thoracic ganglia.

Our results show that mechanosensory modulation differs among WFDN cell types (Figure 2). WFDN_L, which is sensitive to horizontal optic flow towards the ipsilateral side (with respect to the cervical connective), was consistently modulated by airflow stimulation across animals. All other WFDN types were not affected by airflow, except one instance of WFDN_M, which is sensitive to horizontal optic flow towards the contralateral side (Figure 2B,H). The restriction of modulation to horizontal WFDN types could reflect our unilateral airflow configuration, in which only the animal's right wings were stimulated. This lateralised asymmetry could explain the absence of modulation in vertical WFDN types, which may instead require vertical asymmetries. Indeed, airflow was oriented at an angle of attack of 0^o relative to the wing leading edge, producing minimal asymmetry along the vertical axis. If vertical WFDN types are preferentially modulated by vertical airflow components, we predict similar modulation analogous to WFDN_L under non-zero angles of attack.

Alternatively, vertical WFDN types may remain unmodulated regardless of airflow orientation, which could reflect differences in the function of horizontal and vertical WFDN types during normal flight control. Butterflies experience substantial ~10 Hz pitching oscillations with each wing stroke in flight (Fei and Yang, 2016), and vertical WFDNs may function to stabilise these oscillations. Indeed, the difference in temporal frequency maxima for WFDN_V and WFDN_D (Figure 2F) may reflect tuning to the different pitching velocities experienced throughout the wing stroke cycle. Because vertical optic flow and wing mechanosensory feedback vary periodically across wing strokes, additional airflow-induced modulation of vertical WFDNs may introduce response variability that disrupts periodic pitch control. Interestingly, differences between vertical and horizontal motion detection have also been reported in Diptera, with horizontal LPTCs more strongly tuned for observability, whereas vertical LPTCs are biased towards controllability and disturbance sensitivity (Humbert et al., 2025).

What is the function of wing mechanosensation-induced modulation of WFDN_L activity? Spike latency is reduced by ~8%, comparable to the ~6-13% reduction induced by octopamine in flies (Longden and Krapp, 2010, 2009), presenting a notable increase in the dynamic performance of optomotor reflexes. Increased spike rates may in turn increase the reliability of descending control of motor circuits, potentially increasing the probability of muscle contraction for a given descending signal. The preferred mechanosensory frequency of ~60 Hz for WFDN_L suggests that wing mechanosensation is not tuned to the ~10 Hz wing stroke cycle. In fact, aeroelastic wing deformation power declines above ~80–100 Hz across all PCs (Figure 4D). Whilst PC1 exhibits broadband deformation power spanning 10-100 Hz (Figure 4Di), higher-order PCs are concentrated towards 80-100 Hz (Figure 4Dii-iii). The correspondence between aeroelastic wing deformation spectral power and $WFDN_L$ mechanosensitive frequency tuning is consistent with a role in monitoring high-frequency deformation indicative of wing loading and/or aerodynamic perturbations, rather than the wing stroke cycle. $WFDN_L$ was only modulated by mechanosensory input from the wing base, rather than from the distal wing. This suggests that descending visual signals only requires gain modulation without any details of the actual wing deformation. This leaves the fast reflexive circuits within the ganglion, where we found sensory correspondence to distal deformation of the wing, key to more intricate wing deformation-related control.

Overall, our findings demonstrate that wing mechanosensation alone can modulate selected WFDN cell types in butterflies. This modulation does not impact optic flow processing, instead increasing baseline firing rates and reducing spike latency. Future work should investigate whether this modulation depends on airflow asymmetries, and further analysis of butterfly wing deformation dynamics during aerodynamic perturbations may provide additional insight into the functional significance of WFDN modulation. Whether WFDN modulation originates directly from mechanosensory neurons in the thoracic ganglion or via inputs from ascending pathways will require a more detailed analysis of mechanosensory latencies.

Methods

Animals

Experiments were performed on adult Monarch butterflies (*Danaus plexippus*) obtained from a commercial supplier (The Entomologist Ltd, UK). Butterflies were delivered as pupae and reared to eclosion at 25°C, 60% humidity on a 12/12hr light/dark cycle. Adults were fed sugar solution (10% honey in water) daily. Experimental individuals were used within 5-7 days post-eclosion.

Dissection and Electrophysiology

Individuals were immobilised by chilling on ice for five to ten minutes until all voluntary movement ceased. Wings were positioned so that the axis from forewing tip to wing hinge was perpendicular to the body axis, and secured with superglue to prevent voluntary wing movements. Each butterfly was mounted ventral side up in a custom 3D-printed holder using wax that stabilised the body while providing access to the thorax. The head was restrained with fine pins and wax bridges. The proboscis, palps, legs and antennae were removed and heavily waxed to prevent additional sensory input from these structures. The ventral nerve cord was exposed ventrally. During experiments, Lepidoptera saline (in mM: NaCl 147.0, KCl 1.3, $NaHCO_3$ 10.0, $CaCL_2$ 4.0, pH 7.3; (Kinoshita et al., 2015)) was applied to prevent dehydration.

Extracellular recordings were obtained using sharp 2-3 MOhm tungsten microelectrodes (Model: tungsten / 125um / 15–18um / unplated /220-P02 / 15mm; Microelectrodes Ltd., UK) inserted into the animal's right VNC. In butterflies, the mesothoracic and metathoracic ganglia are partially fused, forming a bilobed oval structure with a visible intersegmental boundary (Niven et al., 2008) (Figure 1B). Ganglion interneuron recordings targeted the mesothoracic portion that receives forewing mechanosensory input. A fine hook was placed beneath the ganglion to elevate and stabilise the tissue and to serve as the ground reference electrode. Descending neurons were recorded from the cervical connective as described previously (Supple et al., 2026).

Extracellular action potentials were amplified and digitised via an RHD 16-channel bipolar-input headstage (Intan, USA) using the Open Ephys acquisition system at 30 kHz and monitored in real time with the Open Ephys GUI.

Experimental Setup and Stimuli

Visual stimuli were delivered to a rear projection screen in the insect's frontal visual field, using a LightCrafter DLP3010 (Texas Instruments, USA) at 360 frames per second (fps). A 16x9 cm projection screen was positioned 20 cm from the animal, subtending a visual angle of 44^ox25^o. Visual patterns were generated in MATLAB using Psychtoolbox-3 (Brainard, 1997; Pelli, 1997). Square-wave gratings were used for direction tuning (0-315° in 45° steps, 2 s per direction; temporal frequency = 5 Hz; spatial wavelength = 10°/cycle) and spatiotemporal tuning at a fixed preferred direction (5 s; spatial wavelength = 10°/cycle; temporal frequencies = 0.1-60 Hz). For randomised grating velocity sequences, sine wave gratings were moved along the preferred direction axis with a 0.1-20 Hz band-limited Gaussian noise velocity profile for 10 s. The same velocity sequence was presented a minimum of 10 trials per airflow condition. Visual stimuli timings were synchronised with electrophysiology by recording a blinking trackbox in the corner of the projected image on the electrophysiology AUX channels.

Airflow stimuli consisted of either bulk airflow from the fan, or localised sinusoidal airflow oscillations. Bulk airflow was produced by a fan positioned ~5 cm from the forewing at an angle-of-attack of 0^o relative to the wing leading edge (Figure 1A), generating continuous airflow across the wing surface. Localised sinusoidal airflow oscillations were delivered through a ~2mm diameter tube attached to a small electronic audio speaker driven MATLAB-generated voltage outputs from a NI-DAQ (National Instruments, USA). The tube was positioned either at the forewing base or the distal forewing (located at ~75% spanwise from the base and 50% chordwise). Localised airflow was delivered at a range of frequencies between 4-400 Hz for 1 second per frequency. Airflow pressure exiting the tube was calibrated to equal amplitudes across the stimulation frequency range using a pressure sensor.

Wing deformation was recorded using a single high-speed camera (FLIR BFS-U3-04S2M-CS, configured to 868.8 fps), positioned to view the animals right fore/hindwing from a lateral viewing angle. The camera was synchronised with electrophysiology via an LED trigger controlled by a Teensy microcontroller; LED flashes were visible in the recorded and simultaneously logged in the electrophysiology data.

Data Processing

During the electrode placement, we attempt to isolate units to minimize the need for spike sorting. For post-processing, neural units were detected using a single voltage threshold and manually sorted by spike waveform principal components (PCs) using Spike2 (CED, UK). Units were included for further analysis if they possessed a single distinctive spike waveform PC cluster that was stable throughout the recording session, in addition to minimal inter-spike interval refractory violations under 2 ms. Each recording (electrode penetration) typically yielded one single high-quality neural unit. For each animal, only one instance of a given neuron type was included in our analysis (e.g. if two DNs on separate recordings were sensitive to lateral optic flow, only one instance was included).

Local preferred direction tuning curves were determined from average spike rates of 2 second sequential presentations of gratings moving along eight different directions (Supple et al., 2026). Temporal frequency tuning curves were calculated from average spike rates for 5 second presentations of gratings moving along the preferred direction for temporal frequencies ranging from 0.1 to 60 cycles/sec. Spike triggered averages (STAs) of gratings velocity were calculated by averaging grating velocity within a -100 ms to +50 ms window surrounding each spike time. Neuron latency was calculated from the temporal offset of maximum grating velocity preceding spike time.

Mechano-sensitivity tuning curves were calculated from spike rates in response to sinusoidally-modulated localised airflow stimuli, positioned at either the distal wing or wing base. Wing deformation (displacement) to bulk airflow was estimated from 2D digital image correlation (DIC) using Ncorr (Blaber et al., 2015). Image sequences were first rotated and cropped into a standardised view. The wing region of interest (ROI) was outlined manually on a reference image. Wing ROIs combined fore- and hindwing and were ~96 x 150 pixels. DIC subset radius was 15–20 pixels and subset spacing 6–8 pixels to balance spatial resolution against noise; step analysis and subset truncation were enabled to handle large displacements. 2D wing displacement time series were decomposed via principal component analysis (PCA; mean-centred) to obtain the most prominent deformation modes (Yarger et al., 2025).

For spike triggered averages (STAs) of wing deformation, each PC was z-scored per trial and averaged over a -40 ms to +20 ms window per spike time. STAs of randomised spike times were also calculated to estimate the unconditioned wing deformation prior. Fourier transforms of each PC were calculated for both distal and proximal wing regions, defined by bisecting the wing chordwise at a distance halfway along span.

Statistical Analysis

All data are reported as mean ± SEM, unless stated otherwise. Normality was assessed using the Lilliefors test. Statistical comparisons were performed using paired t-tests (within-subject). Where multiple comparisons were conducted, the familywise error rate was controlled using Bonferroni correction.

Acknowledgements

This work was financially supported by the European Research Council (ERC-StG no.804315 'Vision-In-Flight' to HTL), Biotechnology and Biological Sciences Research Council (grant BB/R002509/1 to HTL, and BB/X002276/1 to HGK), and the Air Force Office of Scientific Research (AFOSR; grant FA8655-23-1-7049 to HGK).

References

Aiello, B.R., Stanchak, K.E., Weber, A.I., Deora, T., Sponberg, S., Brunton, B.W., 2021. Spatial distribution of campaniform sensilla mechanosensors on wings: form, function, and phylogeny. Curr. Opin. Insect Sci., NeuroScience . Special Section on Insects as food and feed (December 2021) 48, 8–17. https://doi.org/10.1016/j.cois.2021.06.002

Blaber, J., Adair, B., Antoniou, A., 2015. Ncorr: Open-Source 2D Digital Image Correlation Matlab Software. Exp. Mech. 55, 1105–1122. https://doi.org/10.1007/s11340-015-0009-1

Brainard, D.H., 1997. The Psychophysics Toolbox. Spat. Vis. 10, 433–436. https://doi.org/10.1163/156856897X00357

Budick, S.A., Reiser, M.B., Dickinson, M.H., 2007. The role of visual and mechanosensory cues in structuring forward flight in Drosophila melanogaster. J. Exp. Biol. 210, 4092–4103. https://doi.org/10.1242/jeb.006502

Chapman, P.D., Burkland, R., Bradley, S.P., Houot, B., Bullman, V., Dacks, A.M., Daly, K.C., 2018. Flight motor networks modulate primary olfactory processing in the moth Manduca sexta. Proc. Natl. Acad. Sci. U. S. A. 115, 5588–5593. https://doi.org/10.1073/pnas.1722379115

Chen, C.-L., Aymanns, F., Minegishi, R., Matsuda, V.D.V., Talabot, N., Günel, S., Dickson, B.J., Ramdya, P., 2023. Ascending neurons convey behavioral state to integrative sensory and action selection brain regions. Nat. Neurosci. 26, 682–695. https://doi.org/10.1038/s41593-023-01281-z

Cheong, H.S.J., Boone, K.N., Bennett, M.M., Salman, F., Ralston, J.D., Hatch, K., Allen, R.F., Phelps, A.M., Cook, A.P., Phelps, J.S., Erginkaya, M., Lee, W.-C.A., Card, G.M., Daly, K.C., Dacks, A.M., 2024. Organization of an ascending circuit that conveys flight motor state in Drosophila. Curr. Biol. CB 34, 1059-1075.e5. https://doi.org/10.1016/j.cub.2024.01.071

Chiappe, M.E., Seelig, J.D., Reiser, M.B., Jayaraman, V., 2010. Walking Modulates Speed Sensitivity in Drosophila Motion Vision. Curr. Biol. 20, 1470–1475. https://doi.org/10.1016/j.cub.2010.06.072

Dahake, A., Stöckl, A.L., Foster, J.J., Sane, S.P., Kelber, A., 2018. The roles of vision and antennal mechanoreception in hawkmoth flight control. eLife 7, e37606. https://doi.org/10.7554/eLife.37606

Fabian, J., Siwanowicz, I., Uhrhan, M., Maeda, M., Bomphrey, R.J., Lin, H.-T., 2022. Systematic characterization of wing mechanosensors that monitor airflow and wing deformations. iScience 25. https://doi.org/10.1016/j.isci.2022.104150

Fabian, S.T., Sondhi, Y., Allen, P.E., Theobald, J.C., Lin, H.-T., 2024. Why flying insects gather at artificial light. Nat. Commun. 15, 689. https://doi.org/10.1038/s41467-024-44785-3

Fei, Y.-H.J., Yang, J.-T., 2016. Importance of body rotation during the flight of a butterfly. Phys. Rev. E 93, 033124. https://doi.org/10.1103/PhysRevE.93.033124

Fischbach, K.-F., Dittrich, A.P.M., 1989. The optic lobe of Drosophila melanogaster. I. A Golgi analysis of wild-type structure. Cell Tissue Res. 258, 441–475. https://doi.org/10.1007/BF00218858

Fujiwara, T., Brotas, M., Chiappe, M.E., 2022. Walking strides direct rapid and flexible recruitment of visual circuits for course control in Drosophila. Neuron 110, 2124-2138.e8. https://doi.org/10.1016/j.neuron.2022.04.008

Fujiwara, T., Cruz, T.L., Bohnslav, J.P., Chiappe, M.E., 2017. A faithful internal representation of walking movements in the Drosophila visual system. Nat. Neurosci. 20, 72–81. https://doi.org/10.1038/nn.4435

Gronenberg, W., Strausfeld, N.J., 1990. Descending neurons supplying the neck and flight motor of Diptera: physiological and anatomical characteristics. J. Comp. Neurol. 302, 973–991. https://doi.org/10.1002/cne.903020420

Haag, J., Wertz, A., Borst, A., 2007. Integration of Lobula Plate Output Signals by DNOVS1, an Identified Premotor Descending Neuron. J. Neurosci. 27, 1992–2000. https://doi.org/10.1523/JNEUROSCI.4393-06.2007

Hardcastle, B.J., Krapp, H.G., 2016. Evolution of Biological Image Stabilization. Curr. Biol. 26, R1010–R1021. https://doi.org/10.1016/j.cub.2016.08.059

Harris, R.A., O'Carroll, D.C., Laughlin, S.B., 1999. Adaptation and the temporal delay filter of fly motion detectors. Vision Res. 39, 2603–2613. https://doi.org/10.1016/S0042-6989(98)00297-1

Hengstenberg, R., 1993. Multisensory control in insect oculomotor systems. Rev. Oculomot. Res. 5, 285–298.

Humbert, J.S., Krapp, H.G., Baeder, J.D., Badrya, C., Dawson, I.L., Huang, J.V., Hyslop, A., Jung, Y.S., Leroy, A., Lutkus, C., Mortimer, B., Nagesh, I., Ruah, C., Walker, S.M., Yang, Y., Taylor, G.K., 2025. Fly motion vision is tuned to maximize signal energy transfer between mechanical input and sensor output.

Ibbotson, M., GOODMAN, L., 1990. Response Characteristics of Four Wide-Field Motion-Sensitive Descending Interneurones IN Apis Melufera. J Exp Biol 148. https://doi.org/10.1242/jeb.148.1.255

Johansson, L.C., Henningsson, P., 2021. Butterflies fly using efficient propulsive clap mechanism owing to flexible wings. J. R. Soc. Interface 18, 20200854. https://doi.org/10.1098/rsif.2020.0854

Jung, S.N., Borst, A., Haag, J., 2011. Flight Activity Alters Velocity Tuning of Fly Motion-Sensitive Neurons. J. Neurosci. 31, 9231–9237. https://doi.org/10.1523/JNEUROSCI.1138-11.2011

Kinoshita, M., Shimohigasshi, M., Tominaga, Y., Arikawa, K., Homberg, U., 2015. Topographically distinct visual and olfactory inputs to the mushroom body in the Swallowtail butterfly, Papilio xuthus. J. Comp. Neurol. 523, 162–182. https://doi.org/10.1002/cne.23674

Krapp, H.G., Hengstenberg, R., 1996. Estimation of self-motion by optic flow processing in single visual interneurons. Nature 384, 463–466. https://doi.org/10.1038/384463a0

Longden, K.D., Krapp, H.G., 2010. Octopaminergic Modulation of Temporal Frequency Coding in an Identified Optic Flow-Processing Interneuron. Front. Syst. Neurosci. 4. https://doi.org/10.3389/fnsys.2010.00153

Longden, K.D., Krapp, H.G., 2009. State-dependent performance of optic-flow processing interneurons. J. Neurophysiol. 102, 3606–3618. https://doi.org/10.1152/jn.00395.2009

Longden, K.D., Muzzu, T., Cook, D.J., Schultz, S.R., Krapp, H.G., 2014. Nutritional state modulates the neural processing of visual motion. Curr. Biol. 24, 890–895. https://doi.org/10.1016/j.cub.2014.03.005

Maimon, G., Straw, A.D., Dickinson, M.H., 2010. Active flight increases the gain of visual motion processing in Drosophila. Nat. Neurosci. 13, 393–399. https://doi.org/10.1038/nn.2492

Maisak, M.S., Haag, J., Ammer, G., Serbe, E., Meier, M., Leonhardt, A., Schilling, T., Bahl, A., Rubin, G.M., Nern, A., Dickson, B.J., Reiff, D.F., Hopp, E., Borst, A., 2013. A directional tuning map of Drosophila elementary motion detectors. Nature 500, 212–216. https://doi.org/10.1038/nature12320

Mohren, T.L., Daniel, T.L., Eberle, A.L., Reinhall, P.G., Fox, J.L., 2019. Coriolis and centrifugal forces drive haltere deformations and influence spike timing. J. R. Soc. Interface 16, 20190035. https://doi.org/10.1098/rsif.2019.0035

Namiki, S., Dickinson, M.H., Wong, A.M., Korff, W., Card, G.M., 2018. The functional organization of descending sensory-motor pathways in Drosophila. eLife 7, e34272. https://doi.org/10.7554/eLife.34272

Nicholas, S., Leibbrandt, R., Nordström, K., 2020. Visual motion sensitivity in descending neurons in the hoverfly. J. Comp. Physiol. A Neuroethol. Sens. Neural. Behav. Physiol. 206, 149–163. https://doi.org/10.1007/s00359-020-01402-0

Niven, J.E., Graham, C.M., Burrows, M., 2008. Diversity and evolution of the insect ventral nerve cord. Annu. Rev. Entomol. 53, 253–271. https://doi.org/10.1146/annurev.ento.52.110405.091322

Olberg, R.M., 1981. Parallel encoding of direction of wind, head, abdomen, and visual pattern movement by single interneurons in the dragonfly. J. Comp. Physiol. 142, 27–41. https://doi.org/10.1007/BF00605473

Parsons, M.M., Krapp, H.G., Laughlin, S.B., 2010. Sensor Fusion in Identified Visual Interneurons. Curr. Biol. 20, 624–628. https://doi.org/10.1016/j.cub.2010.01.064

Pelli, D.G., 1997. The VideoToolbox software for visual psychophysics: transforming numbers into movies. Spat. Vis. 10, 437–442.

Rimniceanu, M., JP, C., MA, F., 2023. Proprioception gates visual object fixation in flying flies. Curr. Biol. CB 33, 1459-1471.e3. https://doi.org/10.1016/j.cub.2023.03.018

Rowell, C.H.F., Reichert, H., 1986. Three descending interneurons reporting deviation from course in the locust. J. Comp. Physiol. A 158, 775–794. https://doi.org/10.1007/BF01324821

Santer, R.D., Rind, F.C., Stafford, R., Simmons, P.J., 2006. Role of an identified looming-sensitive neuron in triggering a flying locust’s escape. J. Neurophysiol. 95, 3391–3400. https://doi.org/10.1152/jn.00024.2006

Schwyn, D.A., Heras, F.J.H., Bolliger, G., Parsons, M.M., Krapp, H.G., Tanaka, R.J., 2011. Interplay between Feedback and Feedforward Control in Fly Gaze Stabilization. IFAC Proc. Vol., 18th IFAC World Congress 44, 9674–9679. https://doi.org/10.3182/20110828-6-IT-1002.03809

Sherman, A., Dickinson, M.H., 2004. Summation of visual and mechanosensory feedback in Drosophilaflight control. J. Exp. Biol. 207, 133–142. https://doi.org/10.1242/jeb.00731

Srygley, R.B., Thomas, A.L.R., 2002. Unconventional lift-generating mechanisms in free-flying butterflies. Nature 420, 660–664. https://doi.org/10.1038/nature01223

Stanchak, K.E., Deora, T., Weber, A.I., Hickner, M.K., Moalin, A., Abdalla, L., Daniel, T.L., Brunton, B.W., 2024. Intraspecific Variation in the Placement of Campaniform Sensilla on the Wings of the Hawkmoth Manduca Sexta. Integr. Org. Biol. 6, obae007. https://doi.org/10.1093/iob/obae007

Strausfeld, N.J., Bassemir, U.K., 1985. Lobula plate and ocellar interneurons converge onto a cluster of descending neurons leading to neck and leg motor neuropil in Calliphora erythrocephala. Cell Tissue Res. 240, 617–640. https://doi.org/10.1007/BF00216351

Strother, J.A., Wu, S.-T., Rogers, E.M., Eliason, J.L.M., Wong, A.M., Nern, A., Reiser, M.B., 2018. Behavioral state modulates the ON visual motion pathway of Drosophila. Proc. Natl. Acad. Sci. U. S. A. 115, E102–E111. https://doi.org/10.1073/pnas.1703090115

Stylman, M., Penz, C.M., DeVries, P., 2020. Large Hind Wings Enhance Gliding Performance in Ground Effect in a Neotropical Butterfly (Lepidoptera: Nymphalidae). Ann. Entomol. Soc. Am. 113, 15–22. https://doi.org/10.1093/aesa/saz042

Supple, J.A., Cerkvenik, U., Ilić, M., Pirih, P., Škorjanc, A., Belušič, G., Krapp, H.G., 2026. Species-specific spectral tuning of motion vision in butterflies. Curr. Biol. 36, 290-306.e5. https://doi.org/10.1016/j.cub.2025.11.037

Suver, M.P., Huda, A., Iwasaki, N., Safarik, S., Dickinson, M.H., 2016. An Array of Descending Visual Interneurons Encoding Self-Motion in Drosophila. J. Neurosci.

Off. J. Soc. Neurosci. 36, 11768–11780. https://doi.org/10.1523/JNEUROSCI.2277-16.2016

Suver, M.P., Mamiya, A., Dickinson, M.H., 2012. Octopamine neurons mediate flight-induced modulation of visual processing in drosophila. Curr. Biol. 22, 2294–2302. https://doi.org/10.1016/j.cub.2012.10.034

Taylor, G.K., Krapp, H.G., 2007. Sensory Systems and Flight Stability: What do Insects Measure and Why?, in: Advances in Insect Physiology. Elsevier, pp. 231–316. https://doi.org/10.1016/S0065-2806(07)34005-8

Tuthill, J.C., Nern, A., Rubin, G.M., Reiser, M.B., 2014. Wide-Field Feedback Neurons Dynamically Tune Early Visual Processing. Neuron 82, 887–895. https://doi.org/10.1016/j.neuron.2014.04.023

Verbe, A., Varennes, L.P., Vercher, J.-L., Viollet, S., 2020. How do hoverflies use their righting reflex? J. Exp. Biol. 223, jeb215327. https://doi.org/10.1242/jeb.215327

Wasserman, S.M., Aptekar, J.W., Lu, P., Nguyen, J., Wang, A.L., Keles, M.F., Grygoruk, A., Krantz, D.E., Larsen, C., Frye, M.A., 2015. Olfactory Neuromodulation of Motion Vision Circuitry in *Drosophila*. Curr. Biol. 25, 467–472. https://doi.org/10.1016/j.cub.2014.12.012

Wertz, A., Borst, A., Haag, J., 2008. Nonlinear Integration of Binocular Optic Flow by DNOVS2, A Descending Neuron of the Fly. J. Neurosci. 28, 3131–3140. https://doi.org/10.1523/JNEUROSCI.5460-07.2008

Wertz, A., Gaub, B., Plett, J., Haag, J., Borst, A., 2009a. Robust Coding of Ego-Motion in Descending Neurons of the Fly. J. Neurosci. 29, 14993–15000. https://doi.org/10.1523/JNEUROSCI.3786-09.2009

Wertz, A., Haag, J., Borst, A., 2009b. Local and global motion preferences in descending neurons of the fly. J. Comp. Physiol. A 195, 1107–1120. https://doi.org/10.1007/s00359-009-0481-0

Yarger, A.M., Maeda, M., Siwanowicz, I., Kajiyama, H., Walker, S.M., Bomphrey, R.J., Lin, H.-T., 2025. Structural dynamics and neural representation of wing deformation. Proc. Natl. Acad. Sci. 122, e2518032122. https://doi.org/10.1073/pnas.2518032122

Yoshida, A., Emoto, J., 2011. Variations in the arrangement of sensory bristles along butterfly wing margins. Zoolog. Sci. 28, 430–437. https://doi.org/10.2108/zsj.28.430

Zhan, S., Qi, Z., Cai, F., Gao, Z., Xie, J., Hu, J., 2024. Oxytocin neurons mediate stress-induced social memory impairment. Curr. Biol. CB 34, 36-45.e4. https://doi.org/10.1016/j.cub.2023.11.037

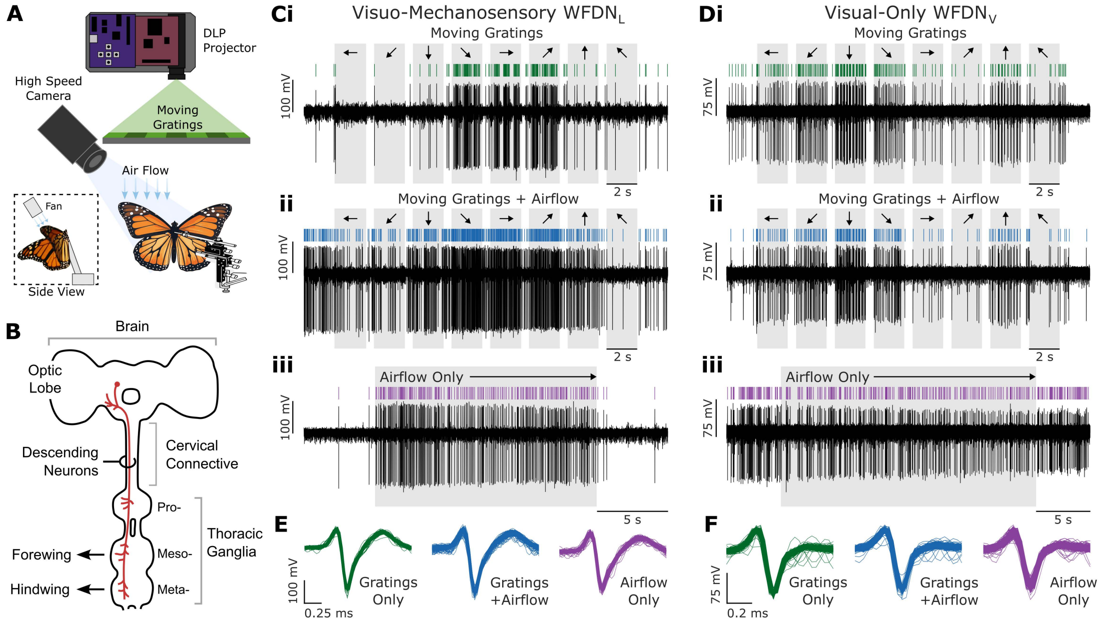

Figure 1: Butterfly wide-field optic flow-sensitive descending neuron (WFDN) responses to visual stimuli and aeroelastic wing deformation.

(A) Experimental setup. Butterflies were mounted ventral-side up with a DLP projected image positioned in the frontal visual field. Butterflies were presented with gratings moving sequentially along different directions with and without airflow directed towards the animal's right forewing, with an angle of attack of 0^{o}. Aeroelastic wing flutters were filmed at 868.8 fps.

(B) Schematic of the butterfly nervous system, viewed from the ventral aspect of the animal, such that the animal's right is on the left-hand side. Extracellular measurements of butterfly descending neurons (DNs, red) were recorded from the animal's right cervical connective.

(C) Example visuo-mechanosensory descending neuron WFDN$_L$ sensitive to both gratings motion and airflow across the wing. (i) Response to gratings moving along eight directions in the frontal visual field without airflow. Arrows indicate direction of grating motion in the animal's frame of reference, i.e., animal's left, down (ventral), right, and up (dorsal). (ii) Response to the same moving gratings with airflow across the wings. (iii) Response to airflow across the wings, without any visual stimulation.

(D) Example visual-only descending neuron WFDN$_V$ that did not exhibit notable response to airflow. Note that both example neurons in C-D were from the same animal. Panels (i-iii) same as (C).

(E-F) Spike sorted units from each stimulus combination in the example traces (C-D).

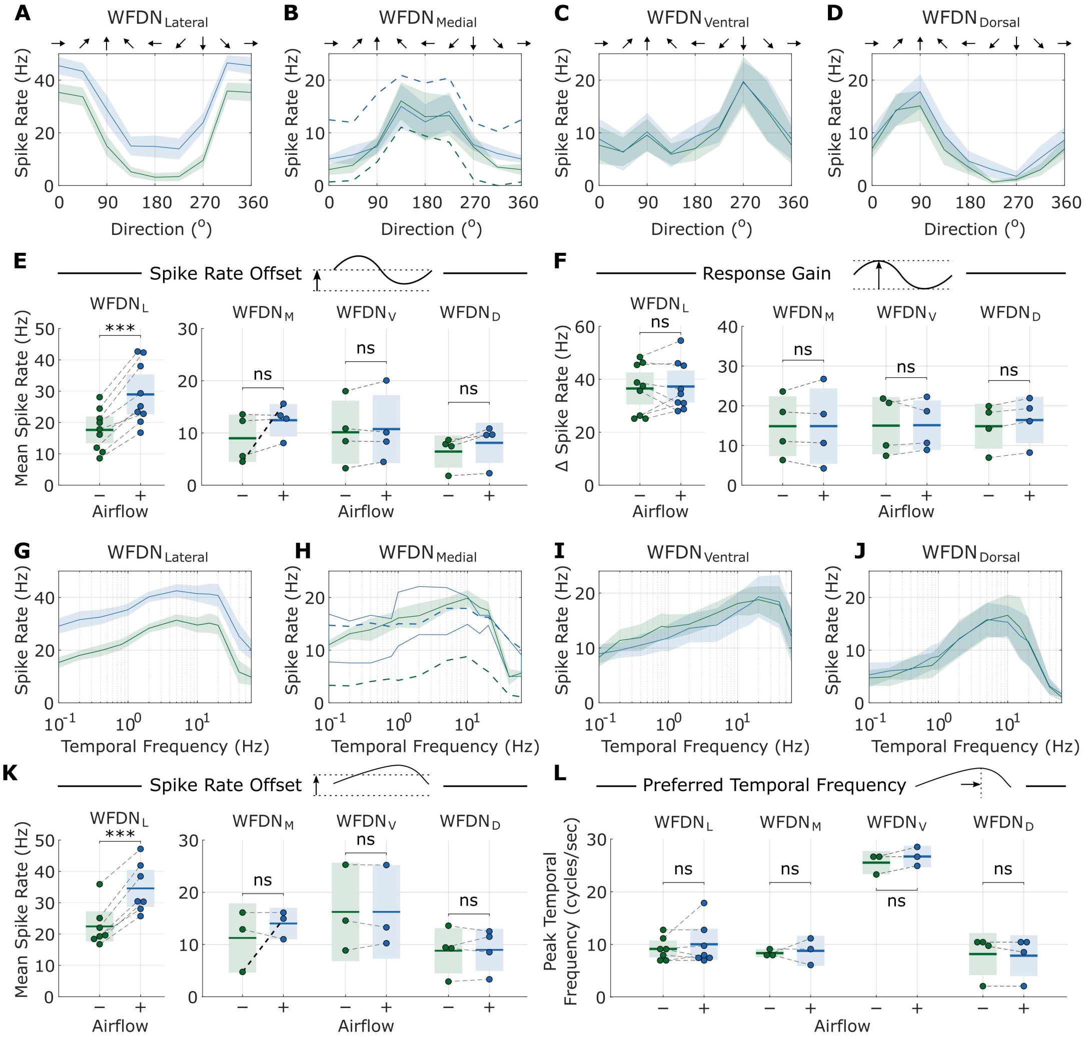

Figure 2: Aeroelastic wing flutter modulates spike rates for selected WFDN cell types.

(A-D) Directional tuning curves for four commonly encountered WFDN cell types sensitive to different directions of local motion in the frontal visual field. (A) WFDN_L: N=9 cells from 9 animals; (B) WFDN_M: N=4 cells from 4 animals; (C) WFDN_V: N=4 cells from 4 animals. (D) WFDN_D: N=4 cells from 4 animals. Response to visual motion without airflow are in green, and vision+airflow in blue. Whilst DNs sensitive to 0^{o} gratings motion (B) tended not to change response when airflow was presented, one animal displayed a substantial increase in spike rate when presented with airflow (indicated by dashed curves). Arrows indicate grating direction in animal's frame of reference: 0^{o} left, 90^{o} dorsal, 180^{o} right, 270^{o} ventral.

(E-F) Statistical analysis of data in panels A-D

(G-H) Descending neuron temporal frequency responses for gratings moving along the preferred direction in the frontal visual field. Response to visual motion without airflow are in blue, and vision+airflow in red. Only two frequency tuning curves were measured under airflow conditions for DNs sensitive to 0^{o} gratings motion (H). Individual tuning curves are shown in solid red lines. An average of three tuning curves is shown for vision-only conditions (blue). Dashed blue/red curves show the response of the airflow-sensitive 0° DN, corresponding to the same neuron in (B).

(K-L) Statistical analysis of data in panels G-H.

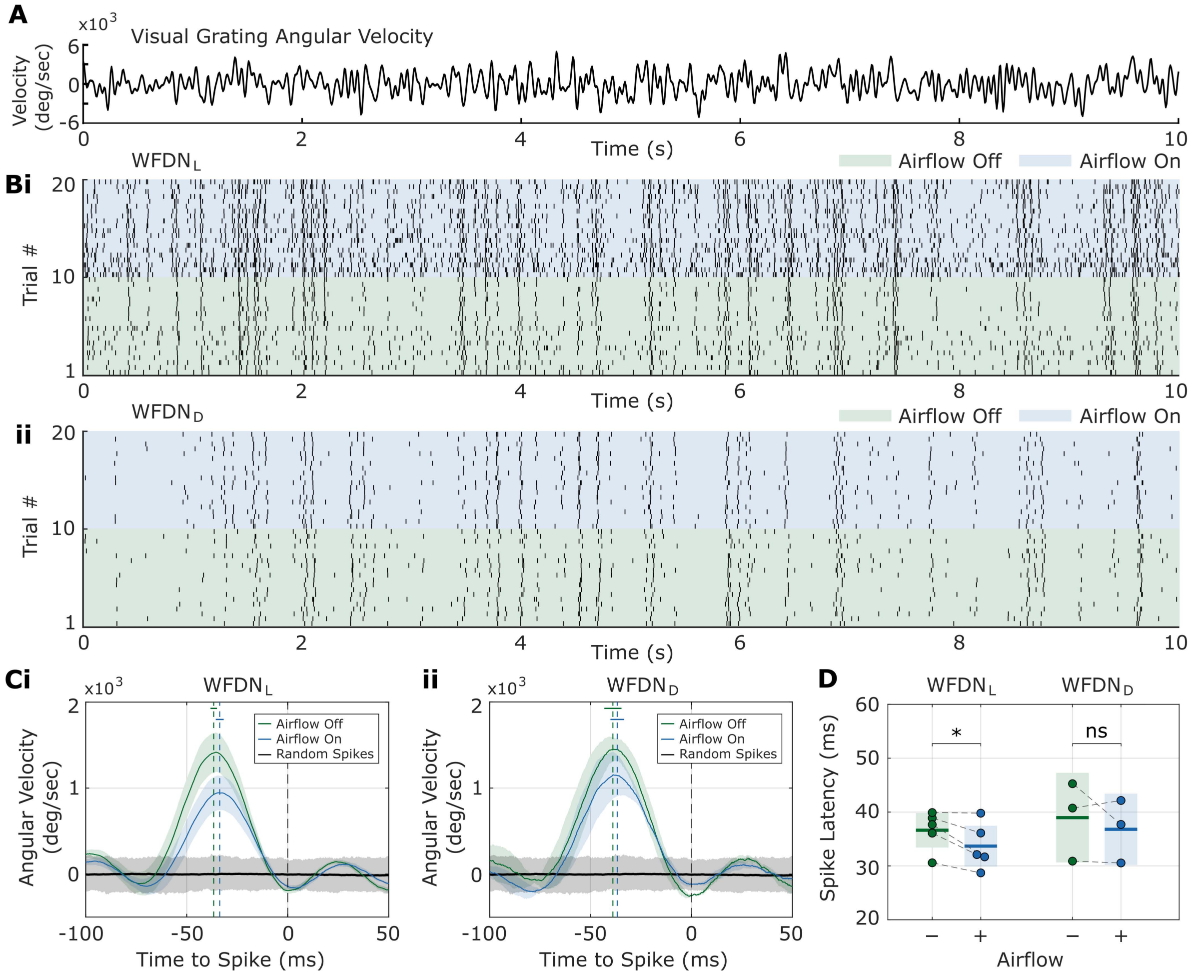

Figure 3: Wing airflow-induced spike rate modulation reduces visual latency

(A) Gratings moved along the preferred direction with band-limited Gaussian-noise velocity.

(B) Example spike raster for (i) $\mathrm{WFDN_L}$ and (ii) $\mathrm{WFDN_D}$ responding to repeated presentations of the gratings stimulus in (A) without (green) and with (blue) airflow across the ipsilateral wing.

(C) Spike-triggered averages (STAs) of grating velocity without (green) and with (blue) airflow for (i) $\mathrm{WFDN_L}$ (N=5 animals) and (ii) $\mathrm{WFDN_D}$ (N=3 animals). Curves show mean±SEM. Spike time is at 0 ms (vertical dashed black line). Vertical dashed green and blue lines show average latency without and with airflow, respectively. Small intersecting horizontal lines show latency SEM. Black line and grey boundary shows STA mean and 95 percentiles for randomised spike times.

(D) Spike latency measurements corresponding to the temporal offset of the STA grating velocity peak preceding the spike time. Lines and shaded regions show mean±SEM, circles show individual animals. Paired t-test $\mathrm{WFDN_L}$ $p=0.04$; $\mathrm{WFDN_V}$ $p=0.51$.

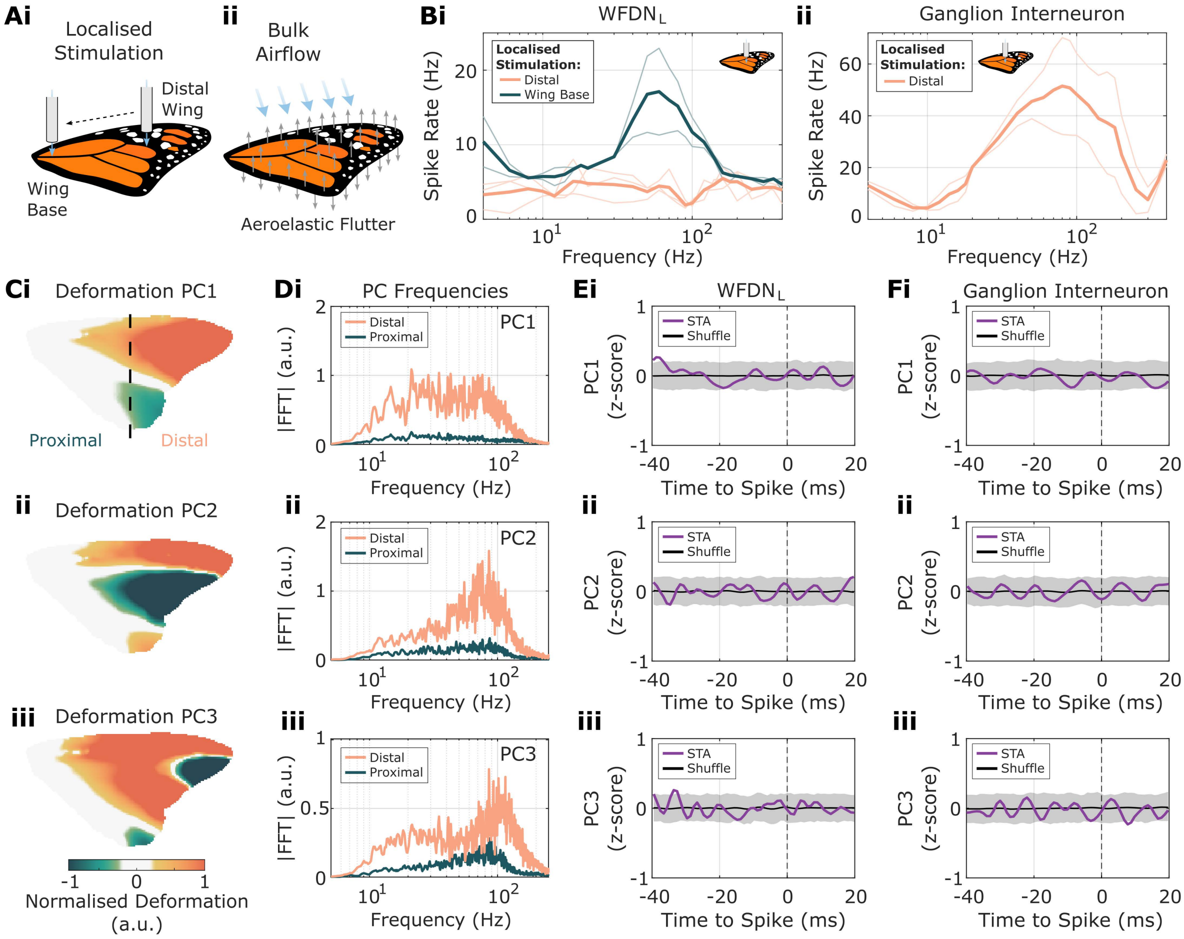

Figure 4: Mechanosensory input to WFDN$_L$ originates from the wing base.

(A) Mechanosensory stimuli consisted of either (i) localised stimulation with sinusoidally modulated air flow, or (ii) bulk airflow across the wing (as used in Figures 1-3). Grey arrows indicate aeroelastic wing deformation. Localised stimulation is applied ventrally, normal to the wing surface; bulk airflow is applied with an angle-of-attack of 0º.

(B) Mechanical frequency sensitivity tuning curves measured from localised sinusoidal airflow stimulation for (i) WFDN$_L$ and (ii) non-visual mechanosensitive interneurons in the meso-thoracic ganglion. Localised stimuli were tested at the distal wing (pink) and wing base (blue). Thick likes show averages, thin lines show individual cells. WFDN$_L$: distal wing N=3 animals, wing base N=2 animals; ganglion interneuron: N=2 animals.

(C) The first three principal components (PCs) of aeroelastic wing deformation under bulk airflow. Delineation of distal and proximal wing regions indicated by dashed line in (i).

(D) Fourier transform of wing deformation PCs in (C).

(E) WFDN$_L$ spike triggered average (STA, purple line) of wing deformation PCs 1-3. Spike time is at 0 ms (vertical dashed black line). Black line and grey boundary show STA and 95 percentiles for randomised spike times. N=1 cell, corresponding to one cell from (Bi).

(F) Mechanosensitive ganglion interneuron STA (purple line) of wing deformation PCs 1-3. Same format as (E). N=1 cell, corresponding to one cell from (Bii).